Research Article Vol. 3, No. 6 / 15 June 2020 / OSA Continuum 1525
OSA CONTINUUM

# Direct comparison of anti-diffracting optical pin beams and abruptly autofocusing beams

DENGHUI LI,[1,8] DOMENICO BONGIOVANNI,[1,2,8] MICHAEL GOUTSOULAS,[3] SHIQI XIA,[1] ZE ZHANG,[4] YI HU,[1] DAOHONG SONG,[1] ROBERTO MORANDOTTI,[2,5] NIKOLAOS K. EFREMIDIS,[1,3,6] AND ZHIGANG CHEN[1,7,*]

[1]*MOE Key Laboratory of Weak-Light Nonlinear Photonics, TEDA Applied Physics Institute and School of Physics, Nankai University, Tianjin 300457, China*
[2]*INRS-EMT, 1650 Blvd. Lionel-Boulet, Varennes, Quebec J3X 1S2, Canada*
[3]*Department of Applied Mathematics, University of Crete, Heraklion, Crete 71409, Greece*
[4]*Aerospace Information Research Institute, Chinese Academy of Sciences, Beijing 100094, China*
[5]*Institute of Fundamental and Frontier Sciences, University of Electronic Science and Technology of China, Chengdu 610054, China*
[6]*Institute of Applied and Computational Mathematics, FORTH, Heraklion, Crete 70013, Greece*
[7]*Department of Physics and Astronomy, San Francisco State University, San Francisco, California 94132, USA*
[8]*These authors contribute equally to this work*
[*]*zgchen@nankai.edu.cn*

**Abstract:** We propose and demonstrate a generalized class of anti-diffracting optical pin-like beams (OPBs). Such beams exhibit autofocusing dynamics while morphing into a Bessel-like shape during long-distance propagation, where the size of their main lobe can be tuned by an exponent's parameter. In particular, their amplitude envelope can be engineered to preserve the pin-like peak intensity pattern. In both theory and experiment, the OPBs are directly compared with radially symmetric abruptly autofocusing beams (AABs) under the same conditions. Furthermore, enhanced transmission and robustness of the OPBs are observed while traversing a scattering colloidal suspension, as compared to both AABs and conventional Bessel beams.

© 2020 Optical Society of America under the terms of the OSA Open Access Publishing Agreement

## 1. Introduction

Diffraction is a natural property of optical beams that causes not only expansion of the beam when propagating in a linear media, but also reduction of the peak intensity value, limiting their potential uses for certain applications. Since the first introduction of Bessel beams [1,2], there have been continued efforts in generating anti-diffracting optical wave packets [3,4]. In this respect, Airy beams [5,6], a well-known representative of the class of non-diffracting optical waves, have received a significant amount of attention, mainly due to their unique intrinsic properties, including diffraction-free propagation [5,6], transverse acceleration [6] and self-healing [7]. The reach of the topic has been further broadened by the possibility to generate different types of self-accelerating wave packets, mostly featuring an Airy-like intensity profile [3]. In particular, abruptly autofocusing beams (AABs) [8–13], which are radially symmetric Airy-like versions, are of interest because they experience a sudden focusing process during their propagation. The beam energy is abruptly focused right before a target while maintaining a low-intensity profile until that moment, making them ideal for surgery and ablation applications [9]. From a physical viewpoint, all non-diffracting beams carry infinite energy. Thus, to be experimentally generated, they must be truncated by an aperture to make the energy content finite. Consequently, diffraction takes place, but the anti-diffractive properties can be maintained for a limited range of

#391878 https://doi.org/10.1364/OSAC.391878
Journal © 2020 Received 2 Mar 2020; accepted 31 Mar 2020; published 1 Jun 2020

OSA CONTINUUM

distances as demonstrated in most of prior experiments. Various research efforts on this field have focused on practical applications of self-accelerating beams, including optical imaging [14–16], particle manipulation [11,17,18], optical communications [19–21], and spatiotemporal light bullets [22,23].

Until recently, the propagation distance of diffraction resisting beams ranged from only a few centimeters to a few meters in experiments. However, last year, Zhang et al. [24] designed and demonstrated "optical pin beams" (OPBs) exhibiting stable wavefronts against diffraction and ambient turbulence during free-space long-distance propagation. Experimentally, OPBs have been proposed only for the specific case of a radially symmetric Airy phase. To broaden the range of potential interests and applications, it is necessary to investigate the possibility to synthesize OPBs that originate from different phase configurations, eventually considering also the additional contribution of properly-structured amplitude modulations. Undoubtedly, light beams exhibiting extended diffraction-free propagation in free space, as well as a constant peak intensity along the propagation distance, are highly desirable and of great value for various applications.

In this work, we theoretically generalize the family of anti-diffracting OPBs, based on varying the exponent's coefficient of the applied radial phase chirp. We demonstrate that OPBs initially display an autofocusing dynamics. After reaching the focal distance, their initial profile reshapes into a Bessel-like beam with its main lobe dimension depending on the propagation distance. The initial autofocusing evolution, together with a propagation dependence of the main-lobe size, represents the most distinctive characteristics of these optical beams when compared to conventional Bessel beams (CBBs). Indeed, while the overall pattern of CBBs is constant during propagation, OPBs are typically characterized by a continuous change of their main-lobe width. Under special conditions, the main-lobe width can also maintain constant while the overall pattern expands. Even though when the beam main-lobe width changes, it is also possible to design the input amplitude in such a way that the peak intensity remains invariant during propagation. Experimentally, unlike other approaches, we generate the OPBs by combining both phase and amplitude modulation in the Fourier space. In addition, we directly compare their propagation dynamics in a strong scattering medium with their counterparts such as AABs and CBBs, demonstrating their superior properties in terms of robustness and intensity stability.

## 2. Theory

In a linear medium, the propagation dynamics of a linearly-polarized optical beam in a cylindrical coordinate system is described under the paraxial approximation condition by the following wave equation:

$$i\frac{\partial\psi}{\partial z}+\frac{1}{2k}\left(\frac{\partial^2\psi}{\partial r^2}+\frac{1}{r}\frac{\partial\psi}{\partial r}+\frac{1}{r^2}\frac{\partial^2\psi}{\partial\varphi^2}\right)=0, \tag{1}$$

where $\psi(r,\varphi,z)$ and $k=2\pi/\lambda$ refer to the electric field envelope and its wavenumber, respectively, while $r$ and $\varphi$ are the radial and azimuthal coordinates, $z$ is the longitudinal distance, and $\lambda$ is the wavelength. General solutions of Eq. (1) are found by using the Fresnel integral:

$$\psi(r,\varphi,z)=\frac{k}{i2\pi z}\int_0^r\int_0^{2\pi}\psi(\rho,\theta,0)e^{ik\frac{r^2+\rho^2-2\rho r\cos(\varphi-\theta)}{2z}}\rho d\rho d\theta, \tag{2}$$

where $\psi(\rho,\theta,0)$ is the input wave profile while $\rho$ and $\theta$ denote the radial and azimuthal coordinates at the input plane, respectively. Here, as a specific case of study, we seek azimuthally-independent solutions of Eq. (1), assuming an Airy-like initial profile, expressed in polar form as:

$$\psi(\rho,\theta,0)=A(\rho)\exp[i\phi(\rho)], \tag{3}$$

OSA CONTINUUM

where $A(\rho)$, $\rho(z)$ and $\phi(\rho) = -kC(\rho/w_\rho)^\gamma$ are real functions, $C_\rho$ is an arbitrary scaling factor, $w_\rho$ is the phase normalization coefficient, and $\gamma$ is the exponent's parameter. Solutions to the Fresnel integral can be found via stationary phase asymptotic calculation by using the initial conditions in Eq. (3) [24]. Applying this method, it is possible to demonstrate that the beam envelope near the symmetry axis is well-approximated by the following expression:

$$\psi(r,z) = \sqrt{\frac{2\pi k}{2-\gamma}}\, A(\rho(z))\, J_0\left(kr(C\gamma z^{\gamma-1})^{\frac{1}{2-\gamma}}\right)\, \left(C\gamma z^{\frac{\gamma}{2}}\right)^{\frac{1}{2-\gamma}} \times \exp\left[i\frac{kr^2}{2z} + (C^2\gamma^2 z^\gamma)^{\frac{1}{2-\gamma}}\frac{k}{2}\left(1-\frac{2}{\gamma}\right) - \frac{\pi}{4}\right], \tag{4}$$

where $J_0$ denotes the zero-order Bessel function, $C = C_\rho/w_\rho{}^\gamma$, and $\rho(z) = (C\gamma z)^{1/(2-\gamma)}$. The full width at half-maximum (FWHM) of OPBs is associated with the central peak of the Bessel function $J_0$, and is defined as:

$$W(z) = \frac{2.27}{k(C\gamma z^{\gamma-1})^{\frac{1}{2-\gamma}}}. \tag{5}$$

The analytical result described by Eq. (4) highlights the properties of such an optical wave. Unlike a standard Bessel beam, the main lobe size depends on the propagation distance $z$. Physically, $\gamma$ can acquire values in the range between 0 and 2. For $1<\gamma<2$, the beam width decreases with $z$, thus resulting in a beam shape that resembles a pin—so the name OPB. Conversely, $W(z)$ increases during propagation for $0<\gamma<1$, while it is $z$-independent when $\gamma$ is unitary. The maximum propagation distance, $z_m$, is estimated by the argument of the amplitude modulation function, $A(\rho)$, through:

$$z_m = \frac{\rho_m{}^{2-\gamma}}{C\gamma}, \tag{6}$$

with $\rho_m$ being the radius of the aperture at the input plane. We note that, in contrast to the case reported in [24], the profile of $A(\rho)$ can be properly engineered, so that for the entire range of distances, the on-axis peak intensity of OPBs preserves a low-varying value given by:

$$A(\rho) = A_{OPB}\rho^{-\gamma/2}\sqrt{\frac{2-\gamma}{2\pi k\gamma C}}, \tag{7}$$

where $A_{OPB}$ is an arbitrary parameter related to the beam peak intensity.

## 3. Simulations

Next, to confirm the theoretical analysis, we performed numerical simulations of OPBs, corresponding to the cases with $\gamma = 0.5$, 1, and 1.5 via the split-step Fourier transform method, applied to Eq. (1). Simulated results are illustrated in Fig. 1 and also compared in Fig. 2 with the analytical solution reported in Eq. (4). At the input plane, we assume that the initial condition in Eq. (3) acquires a zero value inside a ring of radius $\rho_0$. The parameters for the initial amplitude and phase profiles are $A_{OPB} = 5.7\times10^{-3}$, $\lambda = 532$nm, $w_\rho = 1$mm, and $\rho_0 = 0.5$mm. To provide better visualization of the numerical results, the values of the phase scaling parameter $C$ are calculated so that the peak intensity for each case appears at a comparable propagation distance. For $\gamma = 0.5$, 1, and 1.5, $C_\rho$ takes the values 5.96, 3.77, and 3.12μm, respectively. In Figs. 1(a1)–1(c1), we show the numerically obtained longitudinal intensity distributions displaying the propagation dynamics for these three cases of OPBs.

OSA CONTINUUM

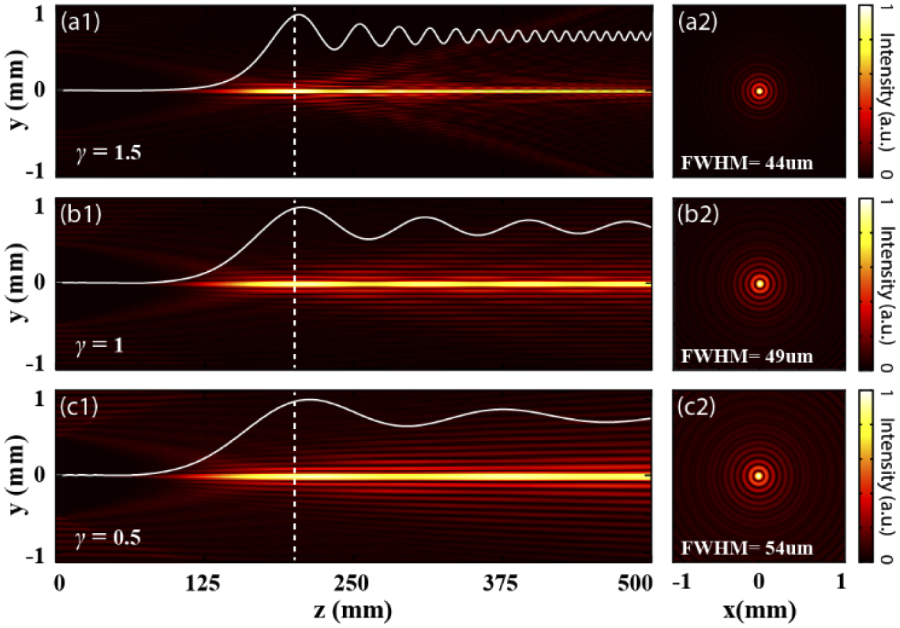


**Fig. 1.** Free-space propagation of OPBs for different values of the parameter $\gamma$. Left panels show longitudinal intensity distributions in the $y$-$z$ plane obtained for (a1) $\gamma = 1.5$, (b1) $\gamma = 1$, and (c1) $\gamma = 0.5$. Solid white curves mark axial intensity evolutions. Right panels depict the corresponding transverse intensity patterns extracted at the plane $z = 200$mm, marked by dashed white lines in the left panels.

In the earlier stage of the evolution, OPBs experience an autofocusing behavior until reaching a focal point, after which the beam power concentrates around the central lobe, by forming a light pin. Transversal intensity cross-sections, retrieved at the distance $z = 200$mm, qualitatively confirm the analytical prediction [Figs. 1(a2)–1(c2)]. Indeed, simulations point out that the OPBs reshape into a Bessel-like beam after the focal distance, displaying an intense main lobe, the transversal size of which changes with the propagation distance according to the parameter $\gamma$. Before the focal distance, the OPBs possess a circular Airy-like shape with an initial main-lobe radius equal to $\rho_0$. Subsequently, the initial radius rapidly decreases during propagation, and the peak intensity abruptly increases reaching the maximum value at the focal distance, which is approximately located at $z = 200$mm. Notably, the white lines, shown in Figs. 1(a1)–1(c1), depict the on-axis peak intensity as a function of $z$. The beam intensity exhibits its maximum value at the focus. After this focal point, it asymptotically decreases with an oscillating trend to a constant value, which is determinate from theory as $I_{\max} = |A_{\mathrm{OPB}}|^2$. The frequency of oscillations decreases for lower values of $\gamma$. In addition, quantitative confirmation of the theoretical analysis is also presented in Fig. 2, where both numerical and analytical intensity profiles taken at the distance $z = 500$mm after the focus are compared. The overlap between these two intensity curves provides clear evidence that numerical profiles are very well-approximated by theoretical calculations, with their mismatch being significantly reduced for longer propagation distances. As expected from theory, for values of $\gamma$ that are greater (or smaller) than 1, the OPB undergoes a shrinking (or broadening) of its main lobe width along the propagation distance, while for $\gamma = 1$, the beam size is independent of $z$. It is worth mentioning that for $\gamma < 1$, even though the beam undergoes spreading during propagation, the main lobe peak intensity appears localized around constant values, which highlights the anti-diffracting capabilities of these OPBs.

OSA CONTINUUM

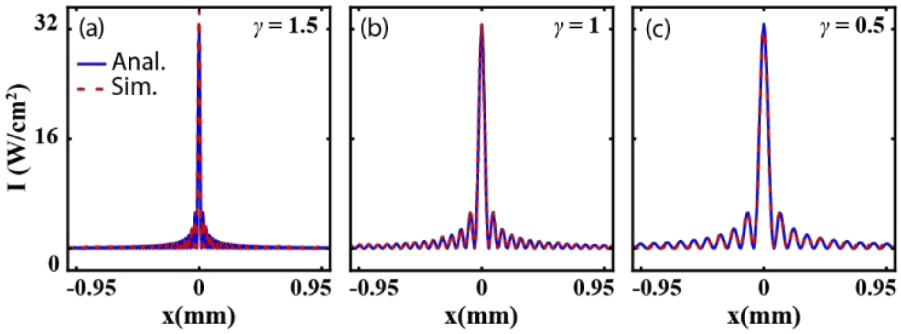


**Fig. 2.** Comparison between analytical (blue lines) and numerical (red lines) intensity profiles along the $x$-direction ($y = 0$) of OPBs extracted at the distance $z = 500$mm for (a) $\gamma = 1.5$, (b) $\gamma = 1$ and (c) $\gamma = 0.5$.

As discussed so far, for each value of $\gamma$, OPBs undergo initial autofocusing dynamics and subsequently Bessel-like reshaping. Since AABs have already attracted a great deal of attention due to their peculiar properties and potential applications [3], we now directly compare the OPBs with the AABs and distinguish their features. We investigate here the dynamics of the AABs mainly devoting attention to the case introduced by Chremmos et al. [10]. The reasons for this choice come from the fact that both beams share a similar initial phase profile. The unique difference is in the phase term of the AABs, which is radially shifted by the radius parameter $\rho_0$ (i.e. $\phi(\rho) = -kC(\rho\text{-}\rho_0)^\beta$). The exponent parameter $\beta$ plays a similar role as $\gamma$ for phase modulation. In the OPB case, no phase shift is applied. Here, the comparison between the two beams is made by numerically simulating their free-space propagation assuming the same phase parameters, and subsequently performing an experimental observation under unchanged conditions. Specifically, the parameters considered are the average power, phase mask scaling and initial radius. Figures 3(a) and 3(b) report the difference between the longitudinal intensity distributions of the OPB with $\gamma = 1.5$ (the same case as in Fig. 1(a)), and the AAB with phase parameter $\beta = 1.5$, $C_\rho = 3.12$μm, $w_\rho = 1$mm, and $\rho_0 = 0.5$mm. The energy scaling between them is carried out by fixing the initial average power to be 10mW. During propagation, as illustrated in Figs. 3(a) and 3(b), both the OPB and AAB maintain a relatively low-intensity profile while abruptly autofocusing and reaching the maximum intensity value at the focal distance, after which they turn into a Bessel-like beam. From stationary phase asymptotic calculations, it can be demonstrated that the collapsing of an AAB related to $\beta = 1.5$ follows a caustic paraboloid surface, created by rotating the curve described in the $y$-$z$ plane by the equation $y(z) = \rho_0 - 0.0055z^2$ [see white lines in Fig. 3(b)] around the propagation axis [10]. It worth noting that, even though the initial radii of the two beams are identical [see Fig. 3(c)], the distance at which the focus takes place for the AAB case is further away than that for the OPB. Furthermore, while the maximum intensity of the OPB is observed to converge to a constant value due to the additional amplitude modulation process, the peak intensity of the AAB is significantly reduced after 500mm of propagation. This is better understood by a direct overlapping of their normalized input and output intensity profiles, as shown in Fig. 3(d). At $z = 500$mm, the main lobe associated with the OPB exhibits a higher peak intensity value as well as narrower beam width than for the AAB case. The combination of these two effects allows for increasing the OPB anti-diffracting ability.

OSA CONTINUUM

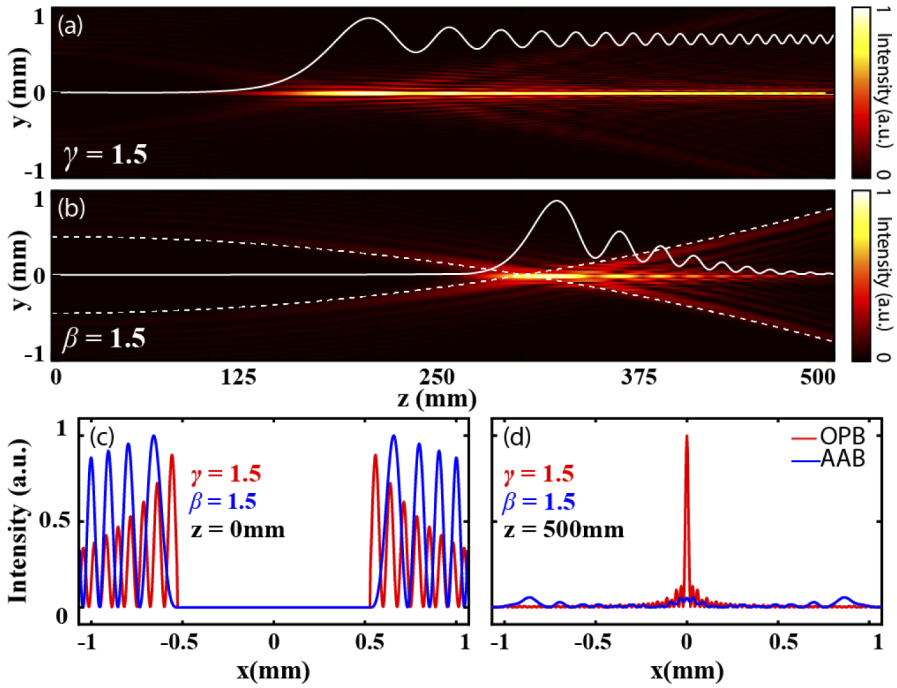


**Fig. 3.** Direct comparison of OPB and AAB characteristics, carried out by numerically simulating the free-space dynamics under the same physical conditions (Parameters: $\rho_0 = 0.5$mm, average power = 1W, $C = 3.12$μm, $\gamma/\beta = 1.5$). (a-b) Longitudinal intensity distributions in the $y$-$z$ plane of the (a) OPB and (b) AAB. (c-d) Normalized intensity profiles in the $x$-direction ($y = 0$) retrieved at (c) $z = 0$mm and (d) $z = 500$mm. Solid lines in (a-b) mark the axial intensity evolutions of the two beams, while dashed lines in (b) display the caustic parabolic trajectory followed by the AAB.

## 4. Experiments

### 4.1. Experimental setup

Besides numerical investigation, we also provide here an experimental characterization of OPBs and AABs in free-space. The setup used for their generation and detection is illustrated in Fig. 4. An incident Gaussian beam (CW laser MGL-F-532 at $\lambda = 532$nm, waist = 2mm), after being expanded by a microscope system (40x, NA = 0.65, $f = 300$mm), illuminates a phase-only spatial light modulator (SLM) device (Holoeye, PLUTO-VIS-016, 1920 × 1080 pixels of 8 × 8μm$^2$ area, 8-bit grey phase levels). A commercial beam splitter (50/50) separates the path of the phase-modulated Gaussian beam reflected by the SLM, from that of the incident beam. At the same time, the beam splitter assures the orthogonal incidence of the input Gaussian beam on the screen of the SLM, guaranteeing the highest phase-modulation efficiency. As reported in Eq. (2), direct generation of OPBs requires the modulation of both amplitude and phase information. In this work, the method used to achieve appropriate initial conditions is the same as the one proposed by Davis et al. [25], where the amplitude and phase profiles are encoded onto a phase-only filter. From a physical viewpoint, the spatial modulation of the phase that is encoded onto the filter leads to a spatial modulation of its diffraction efficiency. Consequently, the energy is selectively transferred between the zero and first diffraction-order, thus allowing the modulation of their amplitude. Compared to the method used in Ref. [24] where the generation of OPBs is carried out in real space, here it is performed in the Fourier domain. To compensate

OSA CONTINUUM

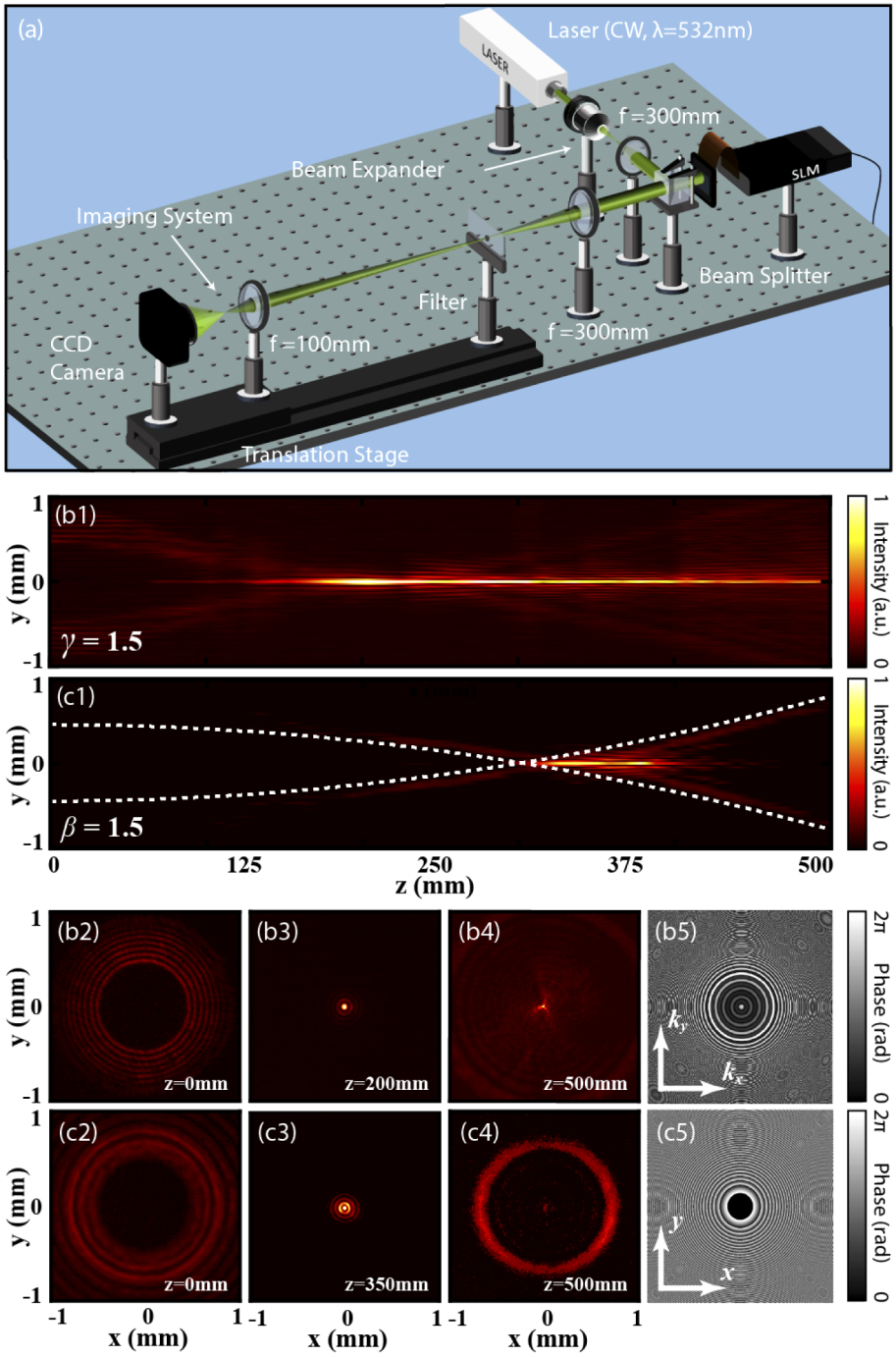


**Fig. 4.** (a) Schematic diagram of the experimental setup used for the generation and detection of OPBs (b1-b5) and AABs (c1-c5) in free space. (b1, c1) Experimental results illustrating longitudinal intensity distributions in the *y*-*z* plane for OPBs and AABs, respectively. (b2-b4, c2-c4) Measured transverse intensity patterns (b2, c2) at the onset distance, (b3, c3) in proximity of the peak intensity planes, and (b4-c4) after 500mm of propagation. (b5, c5) Wrapped phase masks loaded into the SLM device. Dashed lines in (c1) mark the caustic trajectory followed by the AAB [same as in Fig. 3(b)].

OSA CONTINUUM

for the distortion in the encoding process, a correction of the spectral amplitude is additionally made by means of a home-made lookup table. As an example, in Figs. 4(b5) and 4(c5), we show the wrapped SLM phase masks used in our experiments for the generation of the OPBs and AABs, respectively. After shaping, the zero-order diffraction portion of the light beam is subsequently filtered out by means of an opaque mask (0.5mm radius) placed at the focal plane of the lens ($f = 300$mm) that performs the Fourier transform. The characterization is carried out through imaging the beam's transverse patterns at selected longitudinal distances using a standard imaging system, composed by a CCD camera (Coherent LaserCam-HR II $1280 \times 1024$ pixels of $4.6 \times 4.6\mu m^2$ area, 12-bit dynamic range) and a spherical lens ($f = 100$mm), mounted on a translation stage.

### 4.2. Experimental results

In Figs. 4(b1)–4(b5) and 4(c1)–4(c5), we show our experimental results for the propagation of an OPB and an AAB with $\gamma$ and $\beta$ equal to 1.5, respectively. Measures correspond to the same phase profile as in the numerical simulations reported in Fig. 3 and are performed by setting the initial power of the CW laser to 10mW. Evidently, as seen in Figs. 4(b1) and 4(c1), the measured side-view intensity distributions agree very well with their numerical counterparts. A small discrepancy is observed for the OPB case towards the propagation end. That is basically a consequence of the truncation aperture effect introduced by the Gaussian shape of the initial laser beam incident on the SLM device. Consequently, even when the amplitude modulation is applied, the peak intensity tends to decrease during propagation. A way to solve this issue is to include such a Gaussian profile in the amplitude mask designed for the OPB. Moreover, transverse intensity snapshots taken at selected distances highlight the autofocusing property and subsequently the Bessel-like reshaping [Figs. 4(b2)–4(b4) and 4(c2)–4(c4)].

Along with the free-space investigation [26], it is also interesting from the standpoint of both fundamental studies and applications to analyze the dynamics of OPBs propagating in scattering or disordered media. Prompted by these motivations, we further examined and compared the propagation dynamics of the OPB, the AAB, and the CBB over a 350mm distance, including the first 310mm spent in air and the last 40mm inside a cuvette filled with sodium stearate gel. The results presented in Fig. 5 show experimental observations of intensity stability and robustness associated with these three types of beams. The measurement was performed by setting the input average power to 20mW and using the same OPB and AAB as in the free-space case. The CBB was generated by employing the SLM and shaped to possess an input spot size comparable with the other two beams. As illustrated in Figs. 5(a1), 5(b1) and 5(c1), the transverse intensity patterns, captured by the CCD camera at the output facet of the cuvette after a light exposition time of 10s, reveal a Bessel- like profile with a more intense main lobe. Such measured intensity patterns nearly resemble those obtained with the three beams in the homogeneous media, thus qualitatively indicating spatial intensity robustness and stability within scattering colloidal suspensions. For a more detailed evaluation of the spatial stability, we also plotted their normalized intensity profiles along the $x$-direction (in correspondence of the maximum in the $y$-axis). Such intensity profiles were recorded at the input [Figs. 5(a2)–5(c2)] and the output [Figs. 5(a3)–5(c3)] facets of the cuvette at the arbitrary time $t = 8$s. As seen in Fig. 5(a3), the instantaneous spatial intensity profile for the OPB (blue solid curve) is observed to better match the time-average intensity profile (blue dashed line) when compared to the other two cases plotted in Figs. 5(b3) and 5(c3). Besides, we also evaluated the beam's temporal stability by monitoring the output peak intensity varying with time. The temporal average was carried out by taking 200 frames over 10s for each case [Fig. 5(d)]. Clearly, our spatiotemporal observations prove that the OPB performs better than the AAB and the CCB in scattering colloidal suspension media. The OPB not only exhibits more robust intensity stability for localization in space, but also shows a significant reduction of the peak intensity variation with time.

OSA CONTINUUM

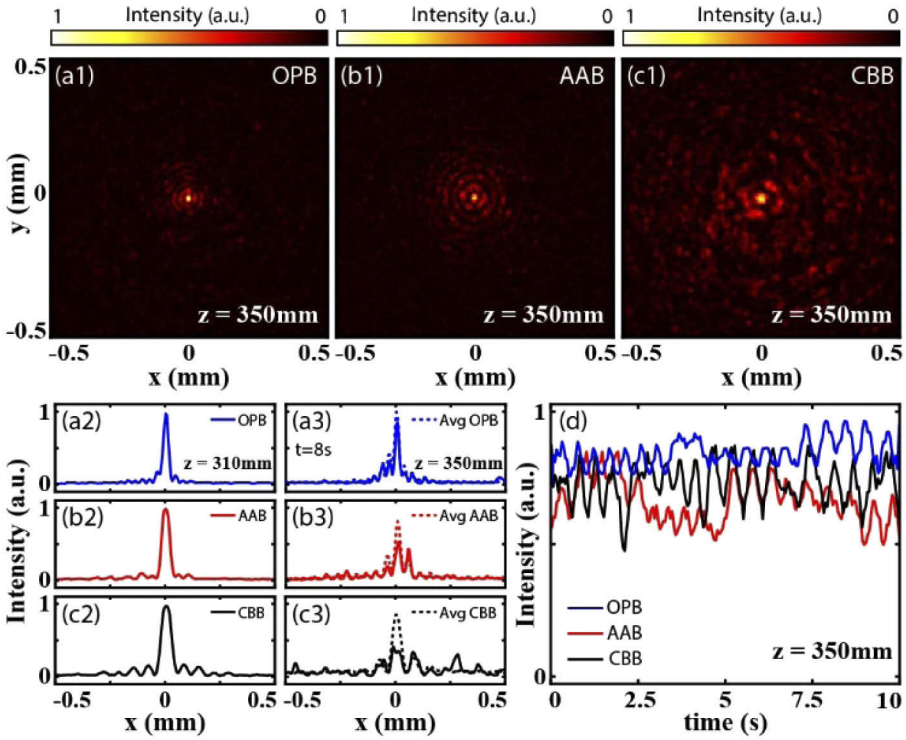


**Fig. 5.** Observation of spatiotemporal stability of (a1-a3) an OPB, (b1-b3) an AAB and (c1-c3) a CBB, propagating through a 40mm-long cuvette filled with sodium stearate gel. (a1, b1 and c1) Output transverse intensity patterns captured by the CCD camera at 10s of light exposition. (a2-a3, b2-b3 and c2-c3) Normalized beam intensity profiles in the $x$-direction measured at the (a2, b2, and c2) input and (a3, b3, and c3) output surface of the cuvette at a time $t = 8$s. (d) Direct comparison of normalized temporal variations of output peak intensities for the three cases under study. For each panel in Fig. 5, solid blue, red and black curves refer, respectively, to the instantaneous spatiotemporal intensity profiles of the OPB, AAB, and CBB, while dashed curves in (a3-c3) display the corresponding average intensity profiles at the output.

## 5. Conclusions

In conclusion, we have generalized the current theory for the class of OPB solutions associated with the paraxial wave equation, by introducing an appropriate modulation of both radial phase and amplitude. An OPB rapidly focuses and transforms into a Bessel-like beam: While its transverse spot size depends on the propagation distance, the axial peak intensity remains almost constant over long distances. Furthermore, we have numerically and experimentally investigated the propagation characteristics of OPBs and AABs, both in free space and in scattering colloidal suspension particles. In free space, under equivalent propagation conditions, OPBs display higher peak intensity values and anti-diffracting properties for longer distances than AABs. In a scattering colloidal suspension, they exhibit robust intensity stability and enhanced transmission with respect to other configurations such as AABs and CBBs. We expect that OPBs can find applications in many areas of optics and photonics such as visible light communication in turbulent and disordered environments, imaging and focusing on scattering biological media, as well as towards shaping laser beams for optical waveguiding, photonic lattice writing and highly localized optical probing.

OSA CONTINUUM

## Funding

National Key Research and Development Program of China ((2017YFA0303800); National Natural Science Foundation of China (11674180, 61575098, 91750204); Natural Sciences and Engineering Research Council of Canada; Ministère de l'Économie, de la Science et de l'Innovation - Québec; State Scholarships Foundation (MIS-5000432); Mitacs (Globalink Research Award).

## Acknowledgments

R.M. is affiliated to UESTC as an adjoining faculty.

## Disclosures

The authors declare no conflicts of interest.

## References

1. J. Durnin, "Exact solutions for nondiffracting beams. I. The scalar theory," J. Opt. Soc. Am. A **4**(4), 651–654 (1987).
2. J. Durnin, J. J. Miceli, and J. H. Eberly, "Diffraction-free beams," Phys. Rev. Lett. **58**(15), 1499–1501 (1987).
3. N. K. Efremidis, Z. Chen, M. Segev, and D. N. Christodoulides, "Airy beams and accelerating waves: an overview of recent advances," Optica **6**(5), 686–701 (2019).
4. X. Weng, Q. Song, X. Li, X. Gao, H. Guo, J. Qu, and S. Zhuang, "Free-space creation of ultralong anti-diffracting beam with multiple energy oscillations adjusted using optical pen," Nat. Commun. **9**(1), 5035 (2018).
5. G. A. Siviloglou and D. N. Christodoulides, "Accelerating finite energy Airy beams," Opt. Lett. **32**(8), 979–981 (2007).
6. G. A. Siviloglou, J. Broky, A. Dogariu, and D. N. Christodoulides, "Observation of accelerating airy beams," Phys. Rev. Lett. **99**(21), 213901 (2007).
7. J. Broky, G. A. Siviloglou, A. Dogariu, and D. N. Christodoulides, "Self-healing properties of optical Airy beams," Opt. Express **16**(17), 12880–12891 (2008).
8. N. K. Efremidis and D. N. Christodoulides, "Abruptly autofocusing waves," Opt. Lett. **35**(23), 4045–4047 (2010).
9. D. G. Papazoglou, N. K. Efremidis, D. N. Christodoulides, and S. Tzortzakis, "Observation of abruptly autofocusing waves," Opt. Lett. **36**(10), 1842–1844 (2011).
10. I. Chremmos, N. K. Efremidis, and D. N. Christodoulides, "Pre-engineered abruptly autofocusing beams," Opt. Lett. **36**(10), 1890–1892 (2011).
11. P. Zhang, J. Prakash, Z. Zhang, M. S. Mills, N. K. Efremidis, D. N. Christodoulides, and Z. Chen, "Trapping and guiding microparticles with morphing autofocusing Airy beams," Opt. Lett. **36**(15), 2883–2885 (2011).
12. R. S. Penciu, K. G. Makris, and N. K. Efremidis, "Nonparaxial abruptly autofocusing beams," Opt. Lett. **41**(5), 1042–1045 (2016).
13. I. D. Chremmos, Z. Chen, D. N. Christodoulides, and N. K. Efremidis, "Abruptly autofocusing and autodefocusing optical beams with arbitrary caustics," Phys. Rev. A **85**(2), 023828 (2012).
14. F. O. Fahrbach, P. Simon, and A. Rohrbach, "Microscopy with self-reconstructing beams," Nat. Photonics **4**(11), 780–785 (2010).
15. T. Vettenburg, H. I. C. Dalgarno, J. Nylk, C. Coll-Lladó, D. E. K. Ferrier, Čižmár, F. J. Tomáš, K. Gunn-Moore, and Dholakia, "Light-sheet microscopy using an Airy beam," Nat. Methods **11**(5), 541–544 (2014).
16. S. Jia, J. C. Vaughan, and X. Zhuang, "Isotropic three-dimensional super-resolution imaging with a self-bending point spread function," Nat. Photonics **8**(4), 302–306 (2014).
17. M. Mazilu, D. J. Stevenson, F. Gunn-Moore, and K. Dholakia, "Light beats the spread: "non-diffracting" beams," Laser Photonics Rev. **4**(4), 529–547 (2009).
18. V. Garces-Chavez, D. McGloin, H. Melville, W. Sibbett, and K. Dholakia, "Simultaneous micromanipulation in multiple planes using a self-reconstructing light beam," Nature **419**(6903), 145–147 (2002).
19. N. Ahmed, Z. Zhao, L. Li, H. Huang, M. P. J. Lavery, P. Liao, Y. Yan, Z. Wang, G. Xie, Y. Ren, A. Almaiman, A. J. Willner, S. Ashrafi, A. F. Molisch, M. Tur, and A. E. Willner, "Mode-division-multiplexing of multiple Bessel-Gaussian beams carrying orbital-angular-momentum for obstruction-tolerant free-space optical and millimeter-wave communication links," Sci. Rep. **6**(1), 22082 (2016).
20. S. Chen, S. Li, Y. Zhao, J. Liu, L. Zhu, A. Wang, J. Du, L. Shen, and J. Wang, "Demonstration of 20-Gbit/s high-speed Bessel beam encoding/ decoding link with adaptive turbulence compensation," Opt. Lett. **41**(20), 4680–4683 (2016).
21. S. Li and J. Wang, "Adaptive free-space optical communications through turbulence using self-healing Bessel beams," Sci. Rep. **7**(1), 43233 (2017).
22. A. Chong, W. H. Renninger, D. N. Christodoulides, and F. W. Wise, "Airy-Bessel wave packets as versatile linear light bullets," Nat. Photonics **4**(2), 103–106 (2010).

OSA CONTINUUM

23. D. Abdollahpour, S. Suntsov, D. G. Papazoglou, and S. Tzortzakis, "Spatiotemporal Airy light bullets in the linear and nonlinear regimes," Phys. Rev. Lett. **105**(25), 253901 (2010).
24. Z. Zhang, X. Liang, M. Goutsoulas, D. Li, X. Yang, S. Yin, J. Xu, D. N. Christodoulides, N. K. Efremidis, and Z. Chen, "Robust propagation of pin-like optical beam through atmospheric turbulence," APL Photonics **4**(7), 076103 (2019).
25. J. A. Davis, D. M. Cottrell, J. Campos, M. J. Yzuel, and I. Moreno, "Encoding amplitude information onto phase-only filters," Appl. Opt. **38**(23), 5004–5013 (1999).
26. C. Vetter, R. Steinkopf, K. Bergner, M. Ornigotti, S. Nolte, H. Gross, and A. Szameit, "Realization of free-space long-distance self-healing Bessel beams," Laser Photonics Rev. **13**, 1900103 (2019).

128.199.88.42 (ts 2020-10-08 08:50:15 )